Supplemental Information

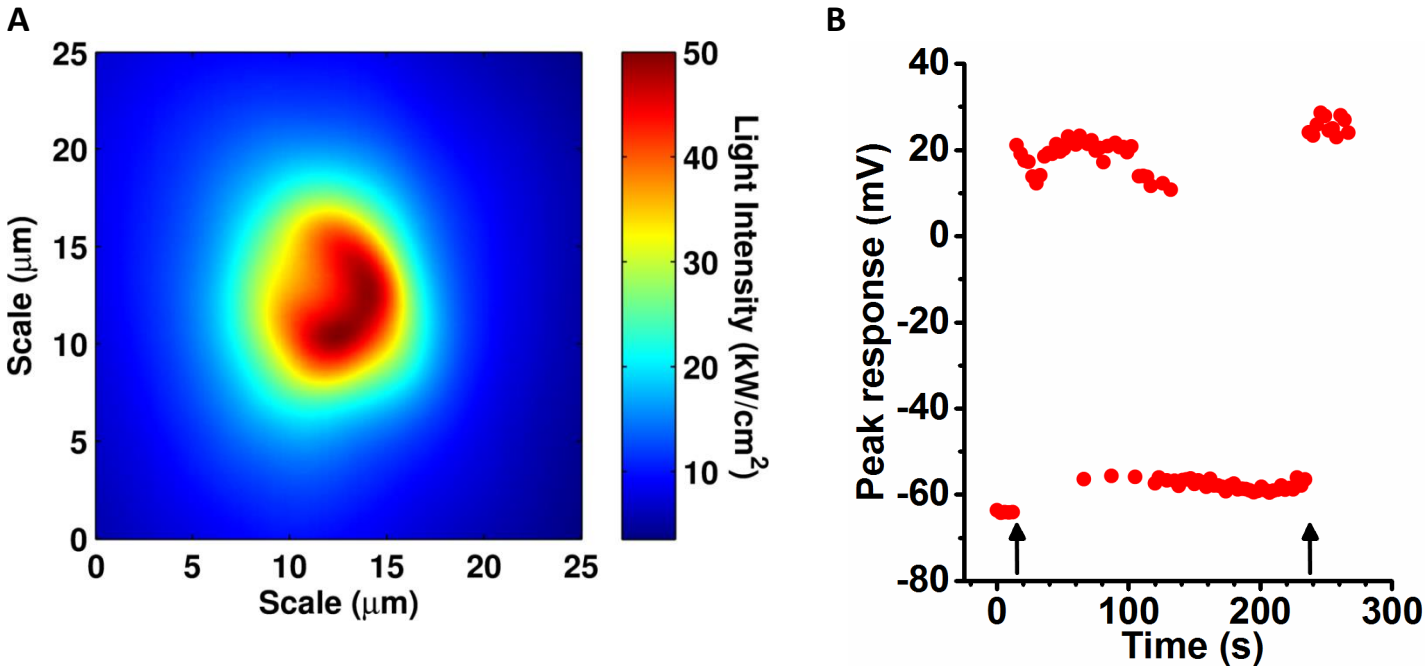

Figure S1, related to Figure 1. Calibration of laser intensity and investigation of diffusion characteristics during experiments with non-functionalized AuNPs. (A) The power distribution of the laser when focused through a 40x microscope objective. The laser was focused onto a slide coated in tetramethylrhodamine, and the resulting fluorescence was imaged with a CMOS camera. The pixel values were summed and normalized to 200 mW, the total power of the laser as measured with a commercial laser power meter. The size imaged by each pixel was calibrated by taking an image of a ruler with the same objective lens. This distribution represents the profile of light seen by the patch clamped neurons in the work when using the laser at full power. The average irradiance was calculated by choosing the half-maximum value as the boundary of the laser spot, roughly corresponding to a circle of 5 μm radius. Within this boundary, the average intensity was 36.2 kW/cm^2 when using full laser power. (B) Diffusion of non-functionalized AuNPs away from DRG neurons causes loss of optical sensitivity. Initially, DRG cells are unresponsive to light as the peak voltage response (the maximum membrane potential reached following a laser pulse) is simply equal to the resting potential. Addition of non-functionalized AuNPs quickly sensitized the cells to light, and they reliably fired action potentials on every pulse. Even without active perfusion washing, however, the non-functionalized AuNPs eventually began to diffuse away from the cells and they lost excitability, firing action potentials with a progressively lower probability over the course of about two minutes. This contrasts with active washing where the cells became completely unresponsive to light within seconds. As expected, addition of a new bolus of AuNPs to the cell restored sensitivity to light. Black arrows show additions of 50 nM AuNP boluses.

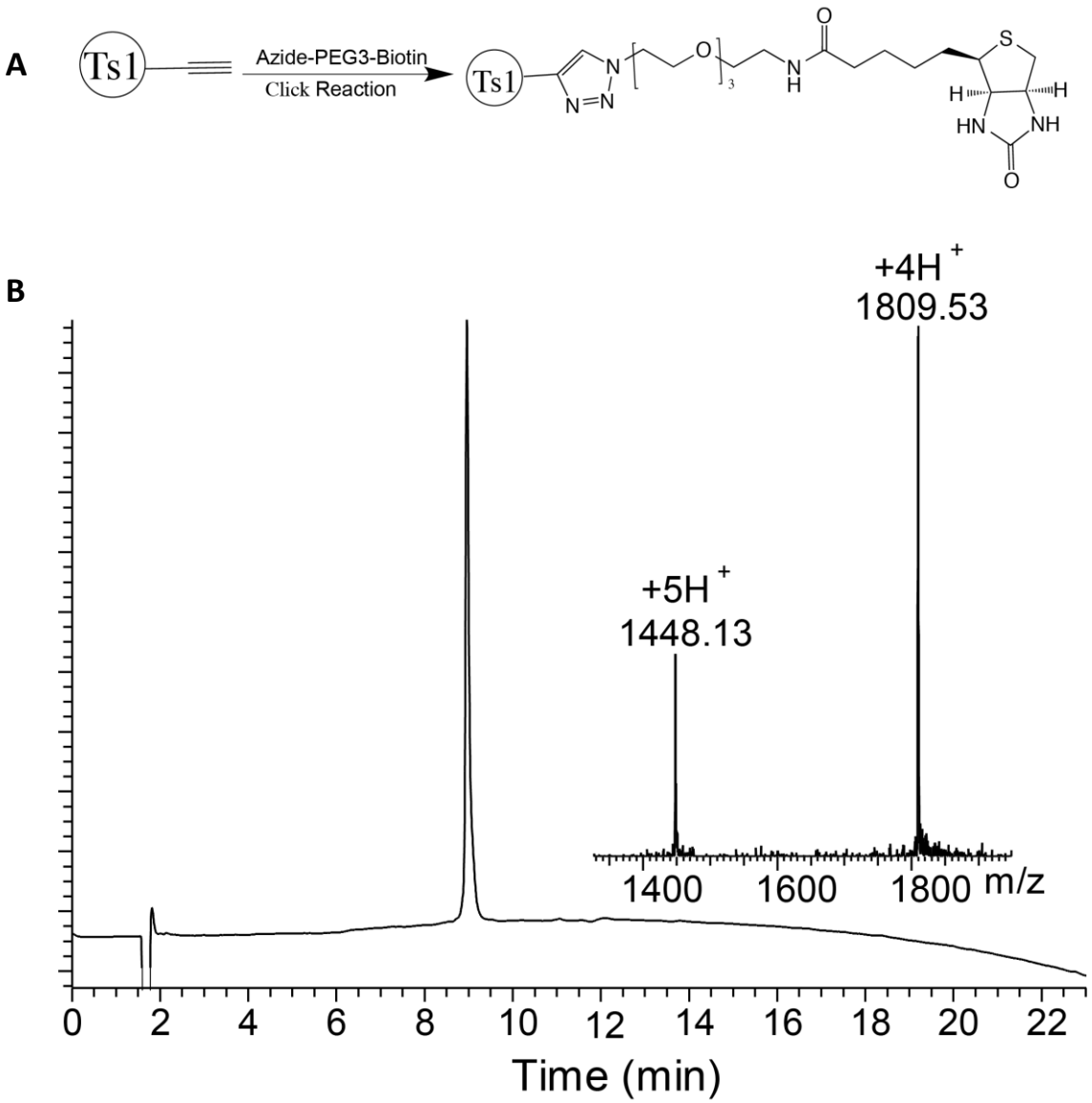

Figure S2, related to Figures 2, 3, and 4. Chemical synthesis of the biotinylated Ts1 used to create the AuNP-Ts1 for the stimulation of DRG neurons and brain slices. (A) Synthetic strategy for the preparation of Ts1-PEG3-Biotin. (B) Purified Ts1-PEG3-Biotin. Inset ESMS Calc. 7235.3 Da (av. isotope composition) Obsd. 7235.4 ± 0.2 Da. The MS data shown were collected across the entire UV absorbing peak.

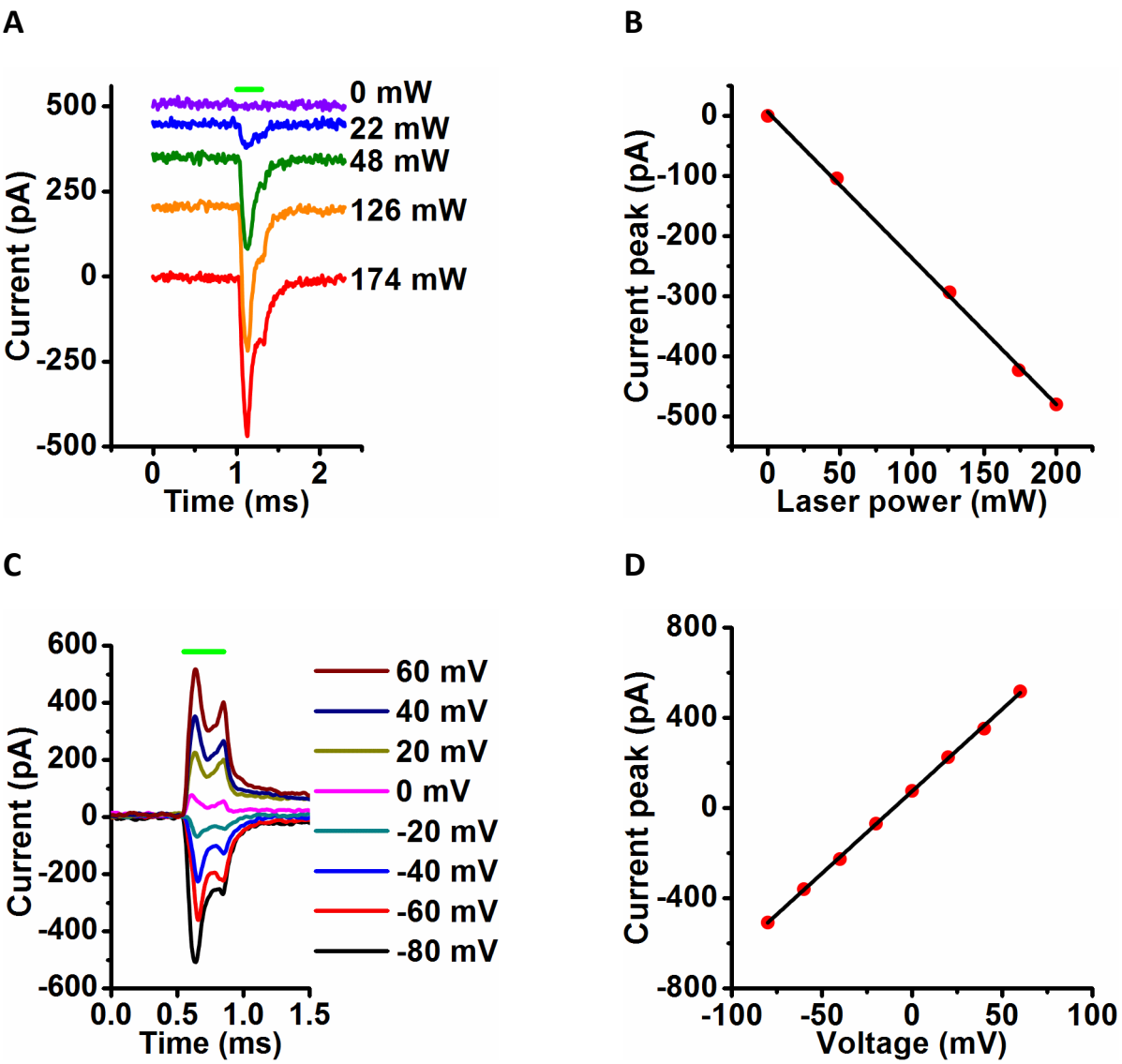

Figure S3, related to Figure 2. Optically-induced currents in DRG neurons induced by AuNP-Ts1 are linear with respect to both laser power and membrane potential when under voltage clamp. (A) Under voltage-clamp at -80 mV, optical stimulation produces an inward current. (B) The laser-induced currents are roughly linear with respect to laser power. (C) A family of voltage-clamp traces at different potentials shows that the amplitudes of the optically-induced currents depend on the membrane potential. (D) The laser-induced currents are linearly dependent on voltage with a reversal potential near 0 mV. Green bars show laser stimuli.

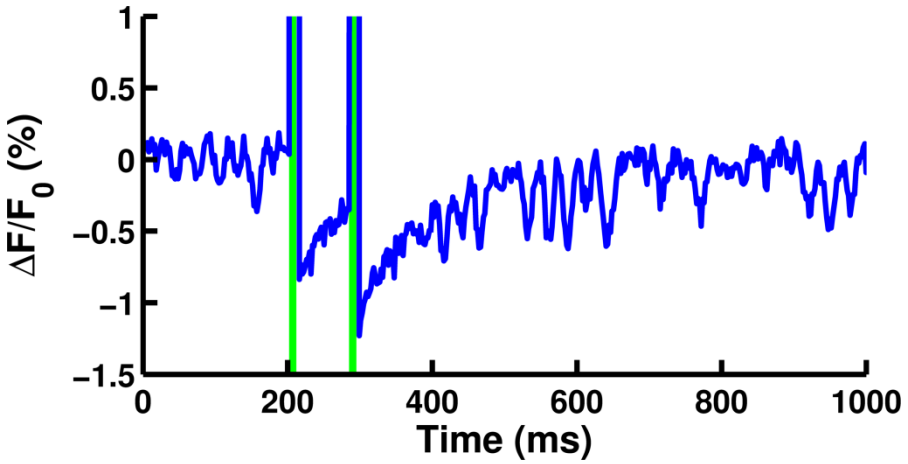

Figure S4, related to Figure 4. Consecutive optical stimuli can produce paired pulse facilitation in hippocampal slices injected with AuNP-Ts1. The brain slice was stimulated with two identical 532 nm laser flashes (225 mW, 10 ms each – green bars) spaced 82 ms apart. The second stimulus produces around 40% more depolarization than the first stimulus.

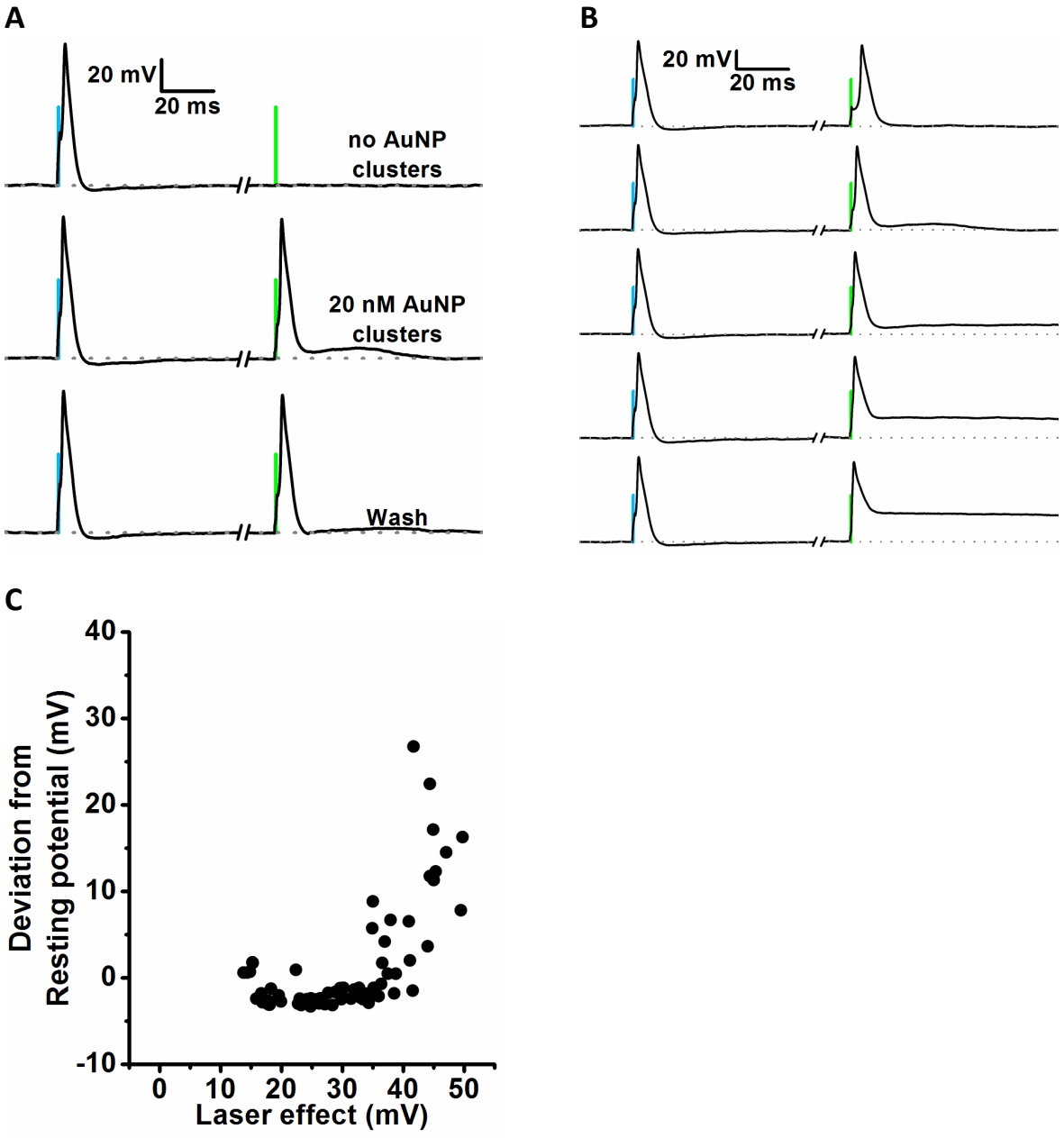

Figure S5, related to Figures 5 and 6. AuNP-TRPV1ab clusters sensitize DRG neurons to light but often lead to laser-induced damage. (A) As with other AuNP-antibody labeling strategies, AuNP-TRPV1ab clusters render DRG cells optically excitable and do not wash out with active perfusion. Electrical stimuli (500 pA, 1 ms – blue bars) and optical stimuli (40 mW, 1ms – green bars) are shown. (B) Laser pulses (40 mW, 1ms – green bars) often cause a persistent depolarization following the action potential when using AuNP-antibody clusters. These are interpreted as membrane damage caused by excessive heating, and the membrane potential usually returns to the initial resting potential with a time course of seconds to minutes. These five traces show the range of damage observed, from near-normal behavior (top) to large and prolonged depolarization (bottom). By contrast, electrical stimuli (500 pA, 1 ms – blue bars) do not cause these pathological depolarizations. (C) The amount of abnormal depolarization remaining 15 ms after a laser pulse (taken as a readout of membrane damage) is strongly correlated with the magnitude of laser-induced depolarization at the beginning of the pulse. Essentially, stronger heating causes larger depolarizing effects, but also leads to greater membrane damage when using AuNP clusters. Interestingly, there seems to be a threshold stimulus size below which no damage is observed. Damage increases sharply with stimulus size above the threshold level.

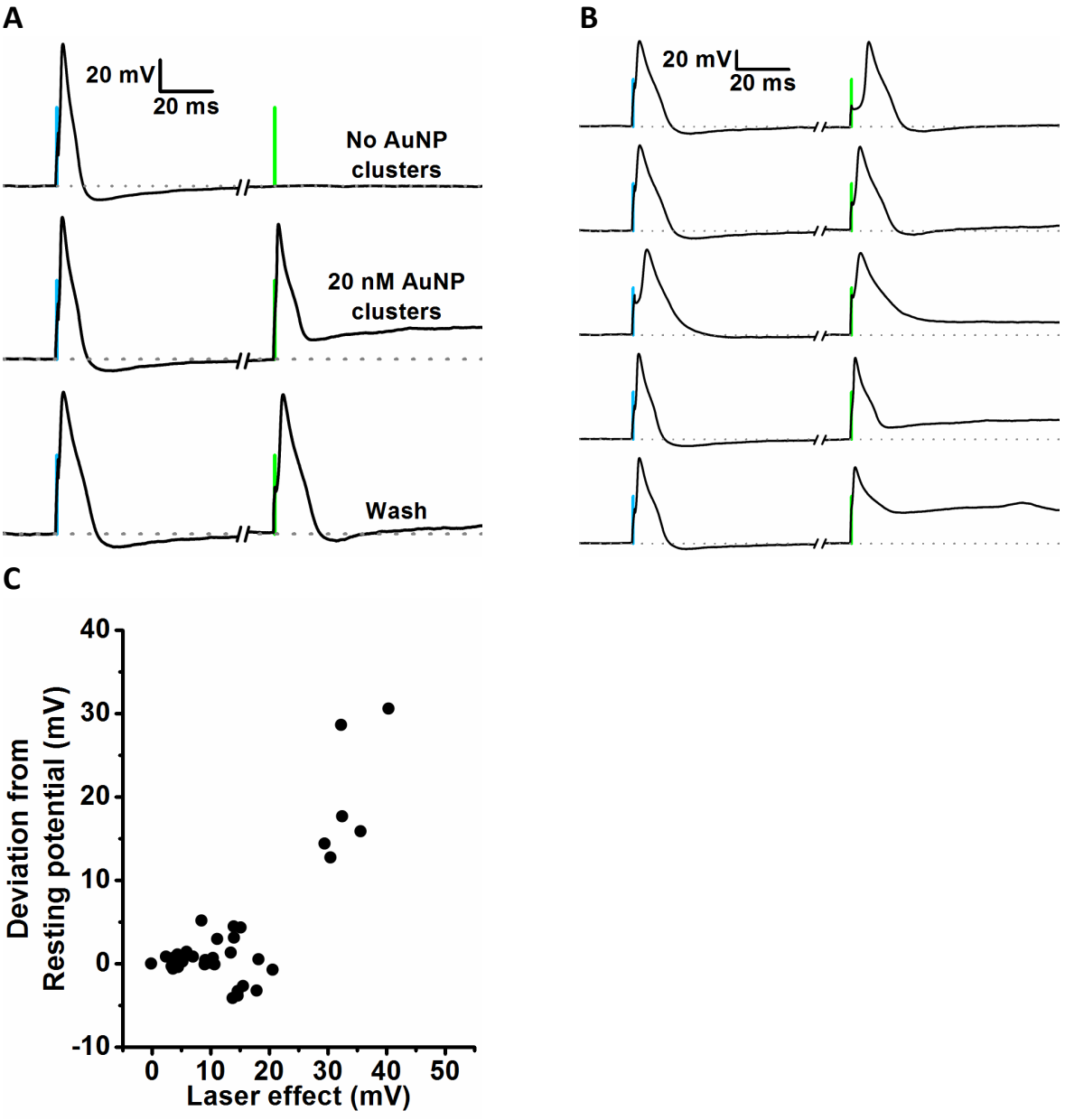

Figure S6, related to Figures 5 and 6. AuNP-P2X$_3$ab clusters behave similarly to AuNP-TRPV1ab clusters. (A) AuNP-P2X$_3$ab clusters sensitize DRG cells to light and do not easily wash out. Electrical stimuli (500 pA, 1 ms – blue bars) and optical stimuli (40 mW, 1ms – green bars) are shown. (B) As with AuNP-TRPV1ab clusters, a wide range of laser-induced damage is often seen following stimulating pulses of light (top – least damage; bottom – most damage). (C) Again, membrane damage depends strongly on stimulus size and seems to exhibit a similar threshold effect. Laser-induced depolarizations below the threshold magnitude (approximately 25 mV in this particular cell) do not lead to abnormal and persistent depolarizations 15 ms after optical stimuli.

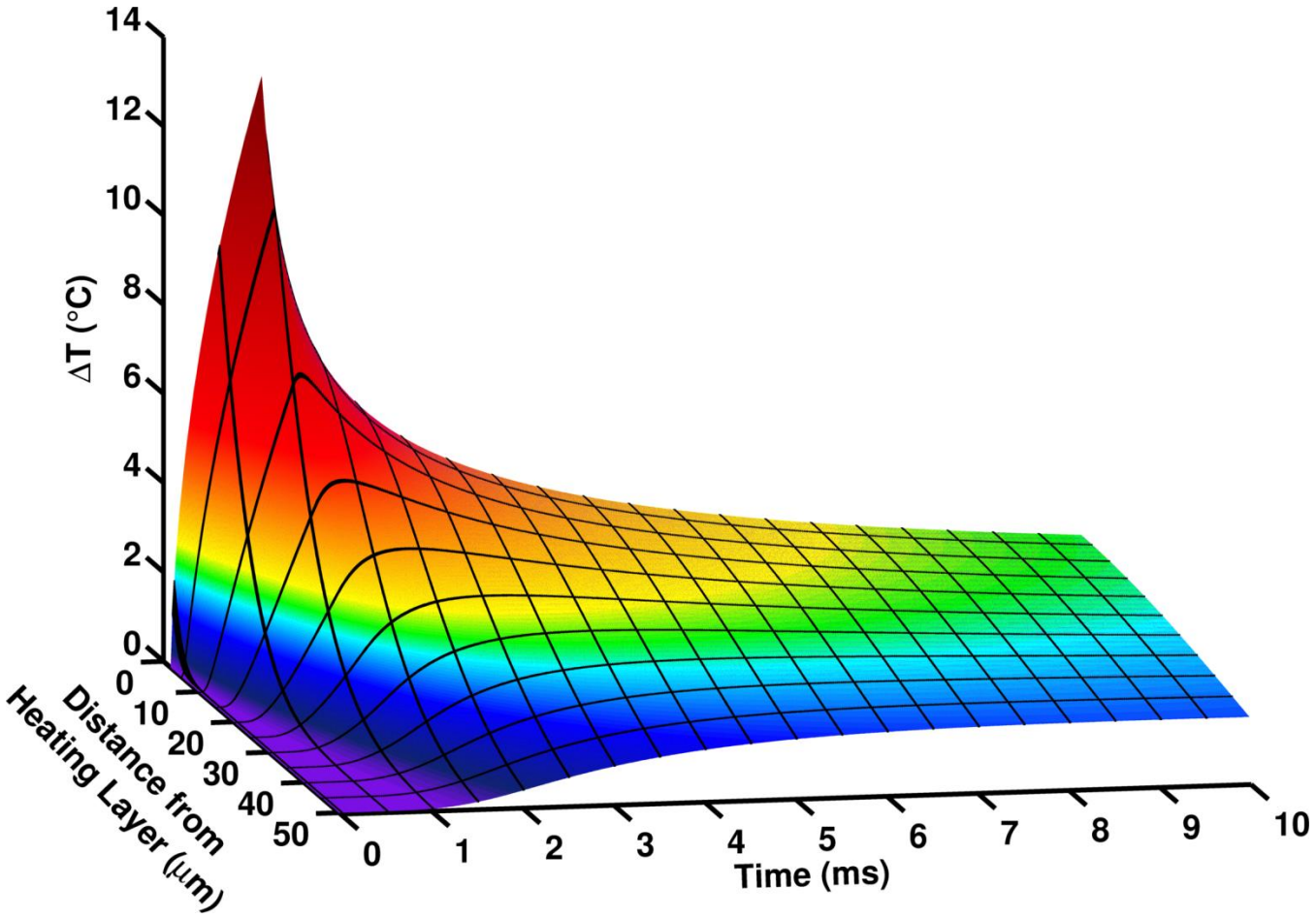

Figure S7, related to Figure 7. The one-dimensional heat diffusion model allows for predictions of temperatures as a function of time and distance from the heating slab. Using the one-dimensional heat diffusion model (see Supplemental Experimental Procedures), changes in temperature were calculated as a function of time and distance from the heating slab. As distance from the heating layer increases, there is an increasing delay before the temperature begins to rise, the kinetics of the temperature increase are slower, and the time to reach peak temperature becomes larger. For this particular simulation, parameters were chosen to model the case of a DRG cell being perfused with 20 nM AuNPs. Accordingly, the heating layer was chosen to be 4 μm thick, the pulse duration was 1 ms at 50% of full laser power, and the fractional volume of the slab occupied by nanoparticles was set as 1 part in 20,000. See also Figure S8.

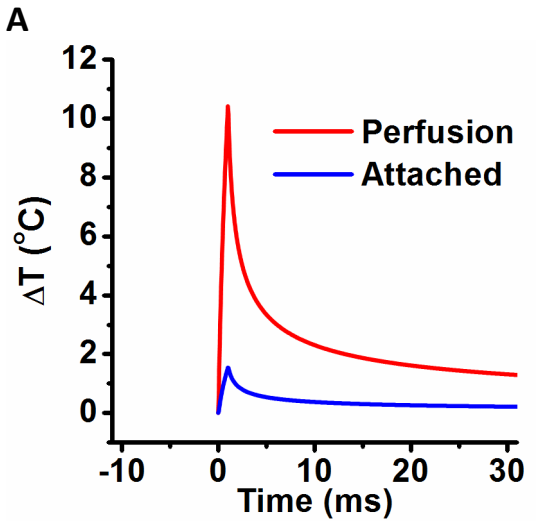

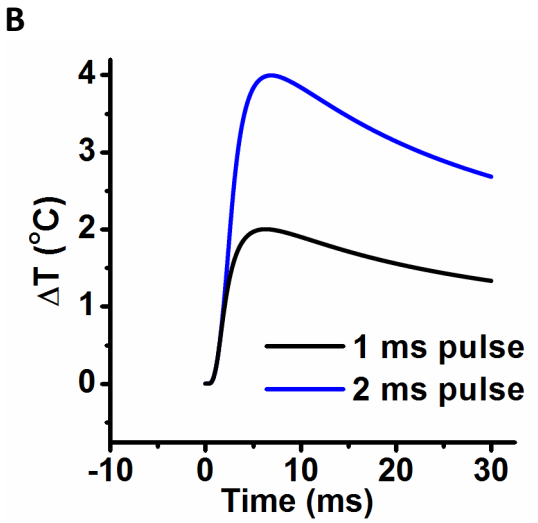

	x	b	V_{frac}	$\frac{I_0}{I_{max}}$	t_1
Perfusion	5 µm	2 µm	1/20,000	1/2	1 ms
Attached	5 µm	10 nm	1/650	1/2	1 ms

	x	b	V_{frac}	$\frac{I_0}{I_{max}}$	t_1
1 ms	50 µm	18 µm	1/20,000	1/16	1 ms
2 ms	50 µm	18 µm	1/20,000	1/16	2 ms

Figure S8, related to Figures 2 and 7. The one-dimensional heat diffusion model qualitatively recapitulates experimental results. (A) The results from DRG cells were modeled for the case where they are being perfused with 20 nM AuNPs as well as after the excess particles are washed out (compare to Figure 2F in the main text). Both simulations used a pulse duration (t_1) of 1 ms and a "measurement location" (x) close to the heating slab, since the measuring pipette was very close to the cell under investigation during the experiment (approximately 2 µm from the edge of the cell, thus perhaps 5 µm from the laser spot). The power used during these experiments was one-half of maximum laser power ($\frac{I_0}{I_{max}}$). For the case of perfusion with 20 nM AuNPs, the fractional volume (V_{frac}) of particles in solution can be calculated to be 1 part in 20,000. We found that given these parameters, a 4 µm-thick heating layer ($2 * b$) most accurately recapitulated the observed data. For the attached nanoparticles case, all parameters were kept the same, except that slab thickness ($2 * b$) was set at 20 nm to model a single-particle-thick heating layer, and V_{frac} was varied to best reproduce the experimental data. In this case, the value of 1/650 corresponds to having approximately 1500 AuNPs attached to a single neuron. While this number is not quantitatively rigorous, it nonetheless is of a very plausible order of magnitude given the number of sodium channels in an average DRG neuron soma. (B) Similar to (A), but simulating the planar lipid bilayer experiment (compare to Figure 7D in the main text). In this case, the measurement location was a much larger and hard-to-estimate distance from the bilayer (since the measurement pipette was vertically above the bilayer rather than lateral to it); we thus estimated 50 µm for this value. Additionally, a relatively large bolus of AuNPs was added via pipettor to the bilayer chamber, likely resulting in a thick heating layer (estimated at 18 µm). The AuNP concentration was again 20 nM, allowing easy calculation of V_{frac}. Finally, the full laser power was used, but through a microscope objective which was 4X less powerful than with the DRG neurons, resulting in $\frac{I_0}{I_{max}} = (\frac{1}{4})^2$. Keeping these parameters identical and varying only pulse duration produced two traces which recapitulate the experimental data well. All traces in this figure were filtered at 1 kHz to better compare with the experimental data (which was identically filtered).

Supplemental Experimental Procedures

Experimental Equipment

Both patch clamp of cells and clamp of painted bilayers were performed using an Axopatch 200B amplifier (Molecular Devices, Sunnyvale, California). The amplifier output was passed through an 8-pole Bessel filter (Frequency Devices, Ottawa, Illinois, model 950L8L) and digitized with an Innovative Integration SBC-6711-A4D4 data acquisition board (Simi Valley, CA). The DAC of the data acquisition board supplied the command voltage to the clamp amplifier. Preps were mounted on a Zeiss IM 35 microscope (Carl Zeiss Microscopy, Thornwood, New York) and visualized through objective lenses ranging from 10x/0.25NA to 40x/0.55NA. Nanoparticles were stimulated with a 532 nm DPSS laser (UltraLasers, Ontario, Canada), and the beam was modulated with an acousto-optic modulator (NEOS Technologies, Gooch & Housego, PLC., Melbourne, Florida). For patch clamp experiments, pipettes were pulled on a Sutter Instruments P-2000 CO_2 laser micropipette puller (Novata, California). Patch pipettes were flame polished using a custom microforge to produce approximately 2 MΩ resistances when filled with internal pipette solution (see 'Solutions' below for all solution compositions). Nanoparticles were delivered via a theta capillary tube pulled to approximately 20 µm tip diameter on a Flaming/Brown pipette puller (Sutter Instruments, model P-87). One side of the theta capillary was filled with an AuNP solution while the other half was filled with bath solution for washing. Each side of the tube was connected to independently-controlled pressurized air. Temperatures were measured by monitoring the resistance in a micropipette with an OC-725A amplifier (Warner Instruments, Hamden, Connecticut). The temperature pipette was pulled to about 2 MΩ and filled with bath solution. Sinusoidal command voltages for measuring membrane capacitance were produced by a function generator (Krohn-Hite, Brockton, Massachusetts, model 1200A).

Brain slices were mounted on an IX71 inverted microscope (Olympus, Center Valley, Pennsylvania) and imaged with an Evolve 128 EMCCD camera (Photometrics, Tucson, Arizona), containing a 128 x128 pixel CCD capable of acquiring images at 500 Hz full-frame. Excitation of ICG was accomplished with a World Star Technologies 780 nm solid-state laser (Toronto, Canada) and the Chroma Technology Corp. Indocyanine Green filter set (Cat #: 49030 ET, Bellows Falls, Vermont), along with a 20X/0.45NA objective lens in the normal inverted microscope position. Stimulation of the nanoparticles was achieved by mounting a 532nm DPSS laser (Laserglow Technologies, Toronto, Canada) and 32X/0.4NA objective on the sample stage and illuminating the brain slices from above.

Materials and Solutions

All concentrations are in mM unless specified otherwise.

Bath solution: NaCl 132, KCl 4, $MgCl_2$ 1.2, $CaCl_2$ 1.8, HEPES 10, glucose 5.5 pH 7.4

Internal pipette solution: NaCl 10, KF 130, $MgCl_2$ 4.5, HEPES 10, EGTA 9, ATP 2, pH 7.3

Artificial cerebrospinal fluid (aCSF): NaCl 125, KCl 2.5, $NaHCO_3$ 26, NaH_2PO_4 1.25, $MgCl_2$ 1.5, $CaCl_2$ 2.5, glucose 10

Bilayer recording solution: KCl 90, HEPES 10, pH 7.4

EBSS: NaCl 132, KCl 5.3, HEPES 10, NaH_2PO_4 1, glucose 5.5, pH 7.4

DMEM: Gibco DMEM, high glucose, HEPES, no phenol red (Life Technologies, Grand Island, New York, Cat #: 21063-029)

PLL: Poly-L-lysine solution, Sigma-Aldrich, St. Louis, Missouri, Cat #: P8920

Trypsin: Worthington, Lakewood, New Jersey, Cat #: TRL3

FBS: Fetal bovine serum, ATCC, Manassas, Virginia, Cat #: 30-2020

Asolectin: Soybean polar lipid extract, Avanti Polar Lipids, Alabaster, Alabama, Cat #: 541602C

Penicillin: Sigma-Aldrich, Cat #: 13750

Streptomycin: Sigma-Aldrich, Cat #: S6501

20 nm AuNP-Streptavidin: Nanopartz, Loveland, Colorado, Cat #: C11-20-TS-50-Buffer

Indocyanine green (ICG): Sigma-Aldrich, Cat #: I2633 (sold as Cardiogreen); stored at 20 mM in DMSO at -80°C

Tetramethylrhodamine-5-maleimide (TMRM): Life technologies, Cat #: T-6027; stored at 20 mM in DMSO at -20°C

Azide-PEG3-Biotin: Sigma-Aldrich, Cat #: 762024

Anti-Rat TRPV1 (extracellular) Antibody, Alomone Labs, Jerusalem, Israel, Cat #: ACC-029

Anti-P2X3 Receptor (extracellular) Antibody, Alomone Labs, Cat #: APR-026

Slide-A-Lyzer MINI Dialysis Devices 20K MWCO, Thermo Scientific, Waltham, Massachusetts, Cat #: 87734

Pierce Antibody Clean-up Kit, Thermo Scientific, Cat #: 44600

EZ-Link NHS-PEG12-Biotin, Thermo Scientific, Cat #: 21312

BupH Phosphate Buffered Saline packs, Thermo Scientific, Cat #: 28372

Methods

Cell Culture Protocol

Glass-bottomed culture dishes were thoroughly cleaned, rinsed with water, dried, and sterilized with UV light. They were then incubated with PLL for 20 min at room temperature, after which they were rinsed with sterile water and stored until use.

Dorsal root ganglia were excised from P1-P3 Sprague-Dawley rats following decapitation and were immediately placed in DMEM on ice. Ganglia were rinsed multiple times with EBSS then digested with EBSS + 0.25% Trypsin for 20 min at 37°C with shaking. Following digestion, the cells were centrifuged and the supernatant removed and replaced with EBSS + 10% FBS to inhibit remaining trypsin. The digested ganglia were then extruded through three glass pipettes of decreasing size to mechanically disperse the cells. The cells were centrifuged a final time and the supernatant replaced with DMEM + 5% FBS. Cells were seeded into the previously prepared PLL-treated culture dishes and allowed to sit undisturbed for 30 min to facilitate DRG cell adhesion to the glass. Finally, the dishes were flooded with DMEM + 5% FBS + 100 U/ml penicillin + 100 ug/ml streptomycin and incubated at 37°C with 5% CO_2 until use.

Hippocampal Slice Preparation Protocol

C57BL/6 mice 65 to 102 days old were anesthetized with isoflurane and decapitated. Their skulls were opened, the cerebella excised from the rest of the brain, and the brains removed from the skull and immediately placed in partially-frozen aCSF. After 5 to 10 minutes, the brains were placed in a vibratome and 350 µm hippocampal slices were cut and immediately placed in aCSF continuously bubbled with carbogen (95% O_2 / 5% CO_2). A mixture was made of 20 nM

AuNP-Ts1 and 2 μM tetramethylrhodamine-5-maleimide (TMRM), and this was loaded into a glass micropipette. Under a microscope, approximately 50 nL of the AuNP-Ts1 solution was injected into the CA1 region of a hippocampal slice immediately before use. This injection was done to bypass the layer of dead cells on the exterior of an acute brain slice. Following the injection, slices were placed in a perfusion chamber on the imaging microscope and stained for 5 minutes with 40 μM indocyanine green (ICG) dissolved in carbogen-bubbled aCSF. Following the staining, carbogen-bubbled aCSF was continuously perfused through the chamber. The 532 nm laser was manually positioned to focus on the nanoparticles by looking for TMRM fluorescence at the injection site excited by the 532 nm light.

Electrophysiology

Neurons were patched under voltage-clamp to monitor the seal resistance. When the giga-seal was achieved, a whole-cell patch clamp configuration was reached by applying a pulse of negative pressure inside the pipette. The ideal series resistance at this point was to be less than three times the initial pipette resistance before touching the neuron. At this point, the amplifier mode was changed to current clamp and the cell excitability was tested with 1 ms current injection pulses of increasing amplitudes. The minimal amplitude needed to trigger action potentials with 70% probability ranged from 300 pA to 700 pA for different cells. The membrane voltage was filtered at 5 kHz and digitized at 20 kHz.

For the voltage clamp experiments, both the membrane capacitance and series resistance were compensated as well as possible. The amplifier current output was filtered at 50 kHz and digitally sampled at 200 kHz.

Painted Bilayer Formation and Electrophysiology

Asolectin lipids were dried in a clean test tube by evaporating the chloroform under a stream of dry nitrogen. The resulting lipid films were placed in a desiccator for at least 1 hour and then dissolved in n-decane to produce a final concentration of 25 mg/ml.

The lipid bilayers were painted in a home-made acetal chambers using a horizontal bilayer configuration. A top chamber, containing a 300 μm orifice, was mounted inside a glass-bottomed lower chamber to allow for laser illumination. The n-decane lipid solution was deposited around the orifice of the top chamber and dried for 10 minutes. Finally, both chambers were filled with bilayer recording solution (see 'Solutions'). Bilayers were painted with an air bubble in a pipettor tip, and their formation and growth monitored under voltage clamp by observing a current response to a voltage ramp. The current data was filtered at 50 kHz and digitized at 200 kHz.

Capacitance Measurement

Capacitances of lipid bilayers were measured by calculating the impedance of the bilayers in response to sinusoidal input voltages. Since the impedance of a capacitor depends inversely on its capacitance, an increasing bilayer capacitance will result in lower impedance and thus an increase in current through the system. Conversely, a decrease in capacitance will cause a decrease in current. Sinusoidal signals were processed by rectifying the waves and then digitally low-pass filtering the result with a Gaussian filtering algorithm. This produced a readout of amplitude versus time while removing the sine wave itself. For these experiments with a 5 kHz carrier sinusoidal applied voltage, we chose a filter cutoff frequency of 1 kHz to strongly attenuate the sinusoid while maintaining features of interest in the signal.

Temperature Measurement

For temperature measurement, pipettes of approximately 2 MΩ were filled with the same solution as in the current bath to avoid an ionic gradient across the pipette tip. They were then placed in as close proximity as possible to either the DRG neuron under investigation or the planar bilayer. Pipette resistances were monitored using a voltage-clamp

amplifier. After each experiment, pipettes were calibrated by placing them in solution next to a thermocouple tip and changing the solution temperature to build a calibration curve between temperature and pipette resistance. Since each pipette has a different shape and resistance, they were calibrated individually after use.

Brain Slice Image Processing

Brain slice data was acquired as movies recorded at 500 Hz (2 ms per frame) on an EMCCD camera. To produce time-dependent traces of activity (Figure 4B in the main text and Figure S4), all pixel values in each frame were averaged together. The resulting fluorescence traces were normalized by taking the average of a region of data from before the laser stimulus (F_0), subtracting this value from all other data points to produce a ΔF, and then finally dividing this value by F_0. This produced the commonly-used normalized fluorescence metric of $\Delta F/F_0$.

The activity images (Figure 4C in the main text) were produced by creating five different averaged images. The first was an average of 180 ms worth of frames from before the stimulus. This was the baseline image. The other four were averages of all frames from four different, consecutive 80 ms windows shortly following the stimulus. For instance, the first of these images was formed by averaging all frames from 20 ms to 100 ms post-stimulus. To reduce pixel noise, all five of these averaged images (pre-stimulus baseline image and four post-stimulus images) were then filtered with a Gaussian low-pass image filter using a standard deviation of five pixels. Finally, the left-most panel in Figure 4C was formed by subtracting the baseline image from the first post-stimulus image and dividing all resulting pixel values by the average fluorescence value of the baseline image. This produces $\Delta F/F_0$ pixel values completely analogous to the time-dependent traces as described above. The other three panels in Figure 4C were formed similarly, but using post stimulus images starting at 100 ms, 180 ms, or 260 ms post-stimulus. All four panels in Figure 4C use the same color scale and no additional image processing was performed beyond the filtering and normalization described above.

Software

Data acquisition, analysis, and modeling were performed using programs written in-house, as well as MATLAB (The MathWorks, Inc.), Mathematica (Wolfram Research), and Origin (OriginLab Corp.).

Mathematical Modeling

Modeling gold nanoparticles

Understanding how the absorption of light by gold nanoparticles leads to membrane depolarization required modeling two distinct but related phenomena. The first step was to model laser-induced heating of the gold nanoparticles and the subsequent diffusion of the heat to a membrane. The final output of this step was a time-course of membrane temperature during and after a laser pulse. Following this, the temperature profile was fed into a second model, described in detail previously (Shapiro et al., 2012), which calculated membrane capacitance as a function of temperature. This capacitance time-course could then be directly converted into membrane currents by elementary electronics calculations.

The first question faced in these models was how to treat the nanoparticles as heat sources. Femtochemistry experiments have shown that the plasmonic absorption of photons and subsequent conversion to heat in gold nanoparticles is a complicated process, involving details such as transiently-differing temperatures between the electron gas of the particle and the crystal lattice of the particle (Link and El-Sayed, 1999). Fortunately, most of these complex dynamics occur on picosecond timescales, vastly faster than neuronal activity. Therefore, at the biologically-relevant timescales for this work (hundreds of microseconds to milliseconds), we treated the particles as simple constant heat sources during laser illumination and assumed that they were always in thermal equilibrium with their immediate

aqueous environment. These assumptions greatly simplified the model and likely introduce little error into the final results.

The initial time points for our heat simulations were chosen to correspond to the beginning of a laser pulse. At this time, the system was assumed to be in thermal equilibrium, so there were constant-temperature initial conditions. Additionally, the system contained internal, time-dependent heat sources (the nanoparticles). During the laser pulses, these behave as constant heat sources as discussed previously; after the end of the pulses they generate zero heat. When added to the heat equation, these sources represent a discontinuous forcing function. This makes the equation most tractable to solving via Laplace transforms, which easily handle forcing functions of this kind.

The next decision was how to model the geometry of the nanoparticles on a membrane. We simulated two distinct scenarios: an idealized case which used symmetry to limit heat diffusion to a single dimension, and a more realistic and general (but more computationally intensive) case with three-dimensional heat diffusion.

One-dimensional heat diffusion

The first scenario considered was a situation where nanoparticles cover an infinitely-large planar membrane. In this scenario, the membrane is treated as being covered in a homogenous layer of "nanoparticle material" of a constant thickness. This entire layer uniformly generates heat during the laser pulse, at a rate dictated by the density of the nanoparticles near the membrane. This set of conditions possesses a 2-dimensional symmetry, and thus there is effectively no lateral heat diffusion or temperature variation in the direction parallel to the membrane. Accordingly, the problem reduces to one of heat diffusion in a single dimension: the direction normal to the plane of the membrane (see Figure below). While such a model is a great simplification of reality and incorporates several assumptions that are not strictly true, such as infinitely-large membranes and particles spread into a homogenous layer, it also greatly reduces both computation times and the number of free parameters in the system. This technique allowed for a rapid survey of many conditions and provided insight into some of the observed features of our data.

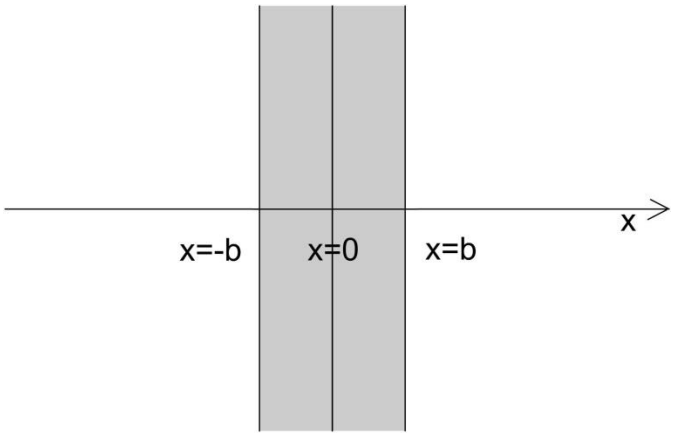

The equation describing this problem is:

$$\frac{\partial^2 T}{\partial x^2} + \frac{A_0}{k} = \frac{1}{\alpha}\frac{\partial T}{\partial t}$$

Where T is the temperature, A_0 is the heat generated during the laser pulse by the particles contained in the slab between $x = -b$ and $x = b$, α is the thermal diffusivity of water (0.143e-6 [m^2 s^{-1}]), k is the thermal conductivity of water (0.6 [W m^{-1} K^{-1}]), x is distance in [m] and t is time in [s]. The pulse of light is applied at $t = 0$ and is removed at $t = t_1$. By applying the Fourier and Laplace transforms we obtained the solutions (for $x > b$):

For $t \leq t_1$:

$$T(x,t) = \frac{A_0\alpha}{k}\left[\sqrt{\frac{t}{\alpha\pi}}\left(x\exp\left[\frac{-x^2}{4\alpha t}\right] - (x-b)\exp\left[\frac{-(x-b)^2}{4\alpha t}\right]\right) + \left(t + \frac{(x-b)^2}{2\alpha}\right)\operatorname{erfc}\left[\frac{x-b}{2\sqrt{\alpha t}}\right] - \left(t + \frac{x^2}{2\alpha}\right)\operatorname{erfc}\left[\frac{x}{2\sqrt{\alpha t}}\right]\right]$$

and for $t > t_1$:

$$T(x,t) = \frac{A_0\alpha}{k}\left\{\left[\sqrt{\frac{t}{\alpha\pi}}\left(x\exp\left[\frac{-x^2}{4\alpha t}\right] - (x-b)\exp\left[\frac{-(x-b)^2}{4\alpha t}\right]\right) + \left(t + \frac{(x-b)^2}{2\alpha}\right)\operatorname{erfc}\left[\frac{x-b}{2\sqrt{\alpha t}}\right] - \left(t + \frac{x^2}{2\alpha}\right)\operatorname{erfc}\left[\frac{x}{2\sqrt{\alpha t}}\right]\right]\right.$$
$$\left. - \left[\sqrt{\frac{(t-t_1)}{\alpha\pi}}\left(x\exp\left[\frac{-x^2}{4\alpha(t-t_1)}\right] - (x-b)\exp\left[\frac{-(x-b)^2}{4\alpha(t-t_1)}\right]\right) + \left(t + \frac{(x-b)^2}{2\alpha}\right)\operatorname{erfc}\left[\frac{x-b}{2\sqrt{\alpha(t-t_1)}}\right] - \left((t-t_1) + \frac{x^2}{2\alpha}\right)\operatorname{erfc}\left[\frac{x}{2\sqrt{\alpha(t-t_1)}}\right]\right]\right\}$$

To compute A_0, we first computed the heat Q generated per unit volume by spherical nanoparticles using the formula of Govorov and collaborators (Govorov et al., 2006).

$$Q = \operatorname{Re}\left[i\omega\frac{\varepsilon(r)-1}{c\sqrt{\varepsilon_0}}I_0\left|\frac{3\varepsilon_0}{2\varepsilon_0+\varepsilon_m}\right|^2\right]$$

Where c is the speed of light, r is the distance from the center of the spherical particle, ε is the complex dielectric constant, ω is the angular frequency of the light, I_0 is the light intensity, ε_m is the dielectric constant of the metal and ε_0 is the dielectric constant of the water. We took the Q produced by each nanoparticle and multiplied it by a factor to account for the fractional volume of the heating slab occupied by nanoparticles (as opposed to non-absorbing aqueous medium) to obtain A_0:

$$A_0 = Q * V_{frac}$$

This process assumes that whatever nanoparticles are in the slab are homogenously spread throughout the volume of the slab. The only difficulty in this process is the determination of the fractional volume occupied by nanoparticles. In the case where a known concentration of particles is present in solution, this value can be calculated directly from the known nanoparticle radius and Avogadro's number. However, in the case where a thin layer is attached to a cell surface, the value must be estimated.

Figure S7 shows an example of a temperature surface output by this model. The gross behavior is as expected, with temperature increasing during the pulse and largely decreasing after. However, it shows that at distances far from the heating layer, the temperature can continue to rise long after the laser pulse ends. Also, it shows that much higher temperatures are reached near to the heating slab than far from it, as one would predict. We used this model to attempt to recapitulate experimental temperature recordings from both DRG neurons and planar lipid bilayers (Figure S8). The model does a good job of qualitatively reconstructing the observed details, although it is not accurate enough to make useful quantitative predictions beyond order-of-magnitude accuracy.

We then computed the capacitance change using the equations in Shapiro et al. Finally, to compute the currents, we solved the membrane circuit under voltage clamp to take into account the limited clamp speed imposed by the series resistance. Like the modeled temperatures, the modeled capacitance changes broadly reflect the experimental results, although they differ from experiment in the fine details.

Three-dimensional heat diffusion

The second scenario we considered was to assume that individual nanoparticles are located at specific locations in an infinite three-dimensional medium. This simulates each particle individually and allows for control over both the density of particles on the surface and the number of layers of particles piled on each other. The solution to this system for a single point-source that turns on at $t = 0$ had been previously derived (Ozisik, 1968), and a modification of this solution allowed for a single point source which also turned off at $t = t_1$. Extending this solution to account for the effects of many individual nanoparticles at specific locations simply amounts to summing the individual contributions of each particle's heat output to the time-dependent temperature at a fixed location, $T(x, y, z, t)$:

For $t \leq t_1$:

$$T(x,y,z,t) = \frac{QV_{NP}}{k} \sum_i \frac{1}{4\pi d_i(x,y,z)} \operatorname{erfc}\left[\frac{d_i(x,y,z)}{2\sqrt{\alpha t}}\right]$$

And for $t > t_1$:

$$T(x,y,z,t) = \frac{QV_{NP}}{k} \sum_i \frac{1}{4\pi d_i(x,y,z)} \left(\operatorname{erfc}\left[\frac{d_i(x,y,z)}{2\sqrt{\alpha t}}\right] - \operatorname{erfc}\left[\frac{d_i(x,y,z)}{2\sqrt{\alpha (t-t_1)}}\right]\right)$$

Where $d_i(x, y, z)$, given by:

$$d_i(x,y,z) = \sqrt{(x-X_i)^2 + (y-Y_i)^2 + (z-Z_i)^2}$$

is simply the Euclidean distance between the point of observation at the coordinate (x, y, z) and the position of the i^{th} nanoparticle, located at (X_i, Y_i, Z_i). All other constants and variables are defined as in the one-dimensional case, with the addition of V_{NP}, the volume of a gold nanoparticle (4.19e-24 [m^3]).

Although the equations describing this model appear simpler than the equations in the one-dimensional model, the summation over all nanoparticles in the system quickly becomes very time-consuming once more than a few thousand particles are being modeled. Practically speaking, this limits the utility of this three-dimensional diffusion model to simulating the case of the DRG neurons after washing, where only a single layer of attached AuNPs is present. From the one-dimensional simulation, we expect the number of particles in this scenario to be on the order of 1,500 (Figure S8), a tractable quantity. We modeled this system a number of times with a variety of specific nanoparticle geometries, and the results are all in broad agreement with the one-dimensional case, although the quantitative specifics vary from simulation to simulation. This corroborates our belief that the one-dimensional model is accurate enough to facilitate qualitative understanding of AuNP heating dynamics, but that neither model is sufficient to support precise quantitative predictions.

As a final test, we modeled the AuNPs as heat-generating spheres of finite size rather than as infinitesimal point-sources of heat using the method of Goldenberg, et al (Goldenberg and Tranter, 1952). The results were nearly identical to the case of point-sources, suggesting that this additional computational burden is unnecessary for the purposes described here.

Chemical Synthesis

Reagents

Azide-PEG3-Biotin was obtained from Sigma-Aldrich; [W50Pra]Ts1.$CONH_2$ was prepared as previously described (Dang et al., 2014). 20 nm AuNP-Streptavidin was obtained from Nanopartz. Anti-Rat TRPV1 (extracellular) Antibody and Anti-P2X3 Receptor (extracellular) Antibody, were obtained from Alomone Labs. Slide-A-Lyzer MINI Dialysis Devices 20K MW

cut-off, Pierce Antibody Clean-up Kit, EZ-Link NHS-PEG12-Biotin, BupH Phosphate Buffered Saline packs, were obtained from Thermo Scientific.

Bath solution was prepared as described above.

Reverse phase HPLC and LC-MS analysis

Analytical reversed phase HPLC and LC-MS were performed using an Agilent 1100 series HPLC system equipped with an online LCQ-Advantage ion trap. Column used was Phenomenex Aeris WIDEPORE 3.6 μm C4, 150 x 4.6 mm. Chromatographic separations were performed using a linear gradient of 20-60% acetonitrile (0.08% TFA) versus water (0.1% TFA) over 20 min with column temperature 40 °C. Flow rates were controlled at 0.9 mL/min. Peptide detection was by UV absorption at 214 nm, and masses were obtained by online electrospray mass spectrometry.

Preparative HPLC

The product from the click reaction was purified using a Phenomenex Aeris WIDEPORE 3.6 μm C4, 150 x 4.6 mm column. A shallow gradient of acetonitrile (0.08% TFA) versus water (0.1% TFA) was used. Flow rates were controlled at 0.9 mL/min. Fractions containing the desired product were collected, identified by analytical LC and mass spectrometry, then combined and lyophilized.

Labeling [W50Pra]Ts1.CONH$_2$ with Azide-PEG3-Biotin.

In a typical reaction, to 2.0 mL of degassed buffer (1 M Guanidine hydrochloride, 200 mM Tris, 40 mM TCEP hydrochloride) was added 80 μL 1 M $CuSO_4$ to generate Cu(I) in-situ; the buffered solution was heated up to ensure the TCEP hydrochloride was fully consumed. After cooling to room temperature, the click reaction buffer pH was adjusted to 8.7 before use. [W50Pra]Ts1.CONH$_2$ (0.2 mg, 29.4 nmol) was dissolved in 240 μL degassed water then Azide-PEG3-Biotin (40 μL of 2.5 mg/mL in DMF) and 120 μL click reaction buffer were added to the solution. The reaction was left for 30 minutes, then another 90 μL of freshly prepared click reaction buffer was added to the reaction mixture. After a further 10 minutes, the reaction product was purified on a C4 analytical column (90 μg, 12.4 nmol, 42.2% yield. Obsd. 7235.4 ± 0.2 Da, Calc. 7235.3 Da (av. isotope composition)). The amount of protein product was determined from the OD 280nm measured on a NanoDrop spectrophotometer.

Conjugation of Ts1-PEG3-Biotin with 20 nm Streptavidin-AuNP:

Ts1-PEG3-Biotin (4 μM, 50 μL in bath solution) and 20 nm AuNP-Streptavidin (54 nM, 50 μL in bath solution) were mixed and shaken well. After 5 hours incubation at 4°C, the mixture was transferred to the 20 MW cut-off MINI dialysis tube and dialyzed against 700 mL bath solution 3 times at 4 °C (4 hours, overnight, 4 hours) with gently stirring to remove non-bound Ts1-PEG3-Biotin. This dialyzed AuNP-Streptavidin-Biotin-PEG3-Ts1 conjugate was used directly for assays.

Biotinylation of Antibodies:

Anti-P2X3 Receptor antibody was reconstituted by adding 100 μL water to give ~2.6 μM antibody solution with 0.5% BSA, 0.025% sodium azide. Sodium azide was removed by dialysis, and BSA was removed by using Pierce Antibody Clean-up Kit. After BSA was removed, 200 μL of 260 nM antibody solution was dialyzed against amine-free phosphate buffered saline (pH 7.5) to exchange the antibody buffer. The antibody solution was then transferred to 0.5 mL Eppendorf tube, and EZ-Link NHS-PEG12-Biotin (10 μL, 50 μM in DMSO) was added, then the mixture was shaken at room temperature for 30 minutes. The mixture was then transferred to a 20 MW cut-off MINI dialysis tube and dialyzed against water for 1 hour at room temperature, then dialyzed against bath solution twice at 4 °C (3 hours, 10 hours) to exchange buffer and to remove non-bound NHS-PEG12-Biotin.

Anti-Rat TRVP1 antibody was reconstituted by adding 100 μL water to give ~2.8 μM antibody solution with 0.5% BSA, 0.025% sodium azide. Sodium azide was removed by doing dialysis, BSA was removed by using Pierce Antibody Clean-up Kit. After BSA was removed, 200 μL of 280 nM antibody solution was dialyzed against amine-free phosphate buffered saline (pH 7.5) to exchange the antibody buffer. The antibody solution was then transferred to a 0.5 mL Eppendorf tube, and EZ-Link NHS-PEG12-Biotin (10 μL, 50 μM in DMSO) was added, then the mixture was shaken at room temperature for 30 minutes. The mixture was then transferred to a 20 MW cut-off MINI dialysis tube and dialyzed against water for 1 hour at room temperature, then dialyzed against bath solution twice at 4 °C (3 hours, 10 hours) to exchange buffer and to remove non-bound NHS-PEG12-Biotin.

Antibody-Biotin conjugation with 20 nm AuNP-Streptavidin:

Each biotinylated antibody (50 μL, 260 nM in bath solution) was mixed with 20 nm AuNP-Streptavidin (50 μL, 54 nM in bath solution) and incubated at 4°C for 1.5 hours. The mixture was then transferred to a 0.5 mL Eppendorf tube. The sample was centrifuged at 12.8 × 1000 rpm for 3.5 minutes, supernatant ~90 μL was removed, and 90 μL bath solution was added to re-suspend the AuNP. Centrifugation was repeated 3 times more to further purify the antibody-AuNP conjugate. The final purified AuNP-Streptavidin-Biotin-Antibody was used for assays.

Supplemental References:

Dang, B., Kubota, T., Correa, A.M., Bezanilla, F., and Kent, S.B.H. (2014). Total Chemical Synthesis of Biologically Active Fluorescent Dye-Labeled Ts1 Toxin. Angew. Chem. *126*, 9116–9120.

Goldenberg, H., and Tranter, C.J. (1952). Heat flow in an infinite medium heated by a sphere. Br. J. Appl. Phys. *3*, 296.

Govorov, A.O., Zhang, W., Skeini, T., Richardson, H., Lee, J., and Kotov, N.A. (2006). Gold nanoparticle ensembles as heaters and actuators: melting and collective plasmon resonances. Nanoscale Res. Lett. *1*, 84–90.

Link, S., and El-Sayed, M.A. (1999). Spectral Properties and Relaxation Dynamics of Surface Plasmon Electronic Oscillations in Gold and Silver Nanodots and Nanorods. J. Phys. Chem. B *103*, 8410–8426.

Ozisik, M.N. (1968). Equation 2-240. In Boundary Value Problems of Heat Conduction, (Scranton, Pennsylvania: International Textbook Company), p. 98.

Shapiro, M.G., Homma, K., Villarreal, S., Richter, C.-P., and Bezanilla, F. (2012). Infrared light excites cells by changing their electrical capacitance. Nat. Commun. *3*, 736.